Role of the Matrix Layers in the Stress-Transfer Mechanism of FRCM Composites Bonded to a Concrete Substrate

C. Carloni[1]; T. D'Antino[2]; L. H. Sneed[3]; and C. Pellegrino[4]

Introduction

In the last few decades, fiber-reinforced polymers (FRPs) composites have been widely used to strengthen RC structures. Externally bonded FRPs have been shown to be an effective strengthening technique for RC structures (Pellegrino and Modena 2009; Salomoni et al. 2011; Carrara et al. 2011; Carloni and Subramaniam 2012; Grace et al. 2012; Carrara and Ferretti 2013). Promising newly developed composite materials are represented by the so-called

fiber-reinforced cementitious matrix (FRCM) composites. They are comprised of high-strength fibers, usually carbon, glass, or polyparaphenylene benzobisoxazole (PBO), embedded within an

inorganic cementitious matrix. In FRCM composites, the fibers are usually bundled, and their pattern can be varied from unidirectional to bidirectional textile weaves or fabrics in an attempt to improve the bond characteristics. Studies in the literature (Täljsten and Blanksvärd 2007; Toutanji and Deng 2007; Hartig et al. 2008; D'Ambrisi and Focacci 2011; Ombres 2012; Pellegrino and D'Antino 2013; D'Ambrisi et al. 2013b) show that FRCM composites potentially represent a valid alternative to FRPs for strengthening and rehabilitating RC structures. The use of an inorganic matrix

[1]Associate Professor, Dept. of Civil, Chemical, Environmental, and Materials Engineering (DICAM), Viale Risorgimento 36, Univ. of Bologna, 40136 Bologna, Italy; formerly, Associate Professor, Univ. of Hartford, West Hartford, CT 06117 (corresponding author). E-mail: christian.carloni@ unibo.it

[2]Postdoctoral Student, Dept. of Civil, Architectural, and Environmental Engineering (DICEA), Univ. of Padova, 35131 Padova, Italy. E-mail: tommaso.dantino@dicea.unipd.it

[3]Associate Professor, Dept. of Civil, Architectural & Environmental Engineering, Missouri Univ. of Science and Technology, Rolla, MO 65409. Email: sneedlh@mst.edu

[4]Assistant Professor, Dept. of Civil, Architectural, and Environmental Engineering (DICEA), Univ. of Padova, 35131 Padova, Italy. E-mail: carlo.pellegrino@unipd.it

in place of the thermosetting organic matrix (usually epoxy) employed for FRP strengthening overcomes some important issues such as the degradation attributable to ultraviolet (UV) and high-temperature exposure and the lack of permeability relative to the concrete substrate.

The literature regarding FRCM composites is still very limited, and a comprehensive study of the stress-transfer mechanism in FRCM-concrete joints is not available. The limited number of studies published report that FRCM-concrete joints fail because of debonding of the fibers within the embedding matrix (Carloni et al. 2013; D'Ambrisi et al. 2012, 2013a). The debonding process is complicated by the so-called telescopic behavior, a mechanism that leads to a differential slip of the fiber filaments within the fiber bundle principally because of the different matrix impregnation of the outer filaments with respect to the core filaments (Banholzer 2004).

The study of the stress-transfer mechanism between the composite and the concrete substrate is of fundamental importance to determine the load-carrying capacity of FRCM-concrete joints. The stress-transfer mechanism between the fibers and the surrounding matrix has been recently studied using a fracture mechanics approach assuming that the shear stresses transferred from the embedded fibers to the two matrix-fiber interfaces are equal (D'Ambrisi et al. 2012; D'Antino et al. 2014). This paper examines this as-sumption and the role of each matrix layer in the stress transfer.

Approach Used in this Paper

The single-lap direct-shear test setup was employed in this work to study the interfacial stress transfer of FRCM composites. One layer of fibers was embedded between two layers of matrix. The internal layer bonded the FRCM composite to the concrete substrate, and the external layer covered the fibers. The overarching goal of this work was to study the role of the internal and external matrix layers in the stress-transfer mechanism. The paper is organized as follows.

1. After a brief description of the experimental results, the characteristics of the idealized load response of the direct-shear tests are highlighted.
2. The macroscale fracture mechanics approach used for the FRP-concrete interface is extended to the matrix-fiber interfaces of

FRCM composites under the hypotheses that the concrete substrate and the matrix layers are rigid.

3. The fracture energy of the matrix-fiber interface is computed from the strain measurements using the aforementioned fracture mechanics approach. The additional hypothesis that the internal matrix layer–fiber and external matrix layer–fiber interfaces have the same behavior is considered.
4. The nonuniform distribution of the applied load among the fiber bundles is discussed.
5. The role of the transversal bundles of the fiber net is discussed to understand whether the force transferred between the fiber filaments and the two layers of matrix is related to the position of the transversal bundles.
6. A comparison between specimens with and without the external layer of matrix is carried out in terms of the debonding load.
7. Finally, three models of the cohesive material laws for the internal matrix layer–fiber and external matrix layer–fiber interfaces are proposed, and the hypothesis that the internal matrix layer–fiber and external matrix layer–fiber interfaces have the same behavior is removed.

Experimental Tests

The bond behavior of FRCM-concrete joints was studied by the authors through an extensive experimental campaign. The push-pull single-lap (direct) shear test setup (Carloni and Subramaniam 2012) was employed in this work (Fig. 1).

The composite was applied on the face of a concrete prism whose surface was sandblasted before the application. Two different con-crete prisms were used, both with a 125×125-mm cross section but different lengths ($L = 375$ or 510 mm). The composite material was comprised of one layer of bidirectional PBO fiber net embedded in two 4-mm-thick layers of a polymer-modified cementitious matrix. The nominal width b^* and average thickness t^* of one longitudinal fiber bundle were 5 and 0.092 mm, respectively. It should be noted that t^* defined in this paper is different from the equivalent thickness of the fabric given by the manufacturer. The equivalent thickness provided by the manufacturer is obtained by assuming that the fibers

are spread evenly over the entire width of the composite rather than bundled. In this paper, t^* represents the thickness of the fiber bundle, which is assumed to have a rectangular cross section of width b^*. The matrix was applied only on the region of the concrete surface that corresponded to the bonded area to bond the composite to the concrete substrate and embed the fibers (Fig. 1). The me-chanical characteristics of the concrete, matrix, and fiber employed are reported in D'Antino et al. (2013, 2014) and are provided in Fig. 1(c).
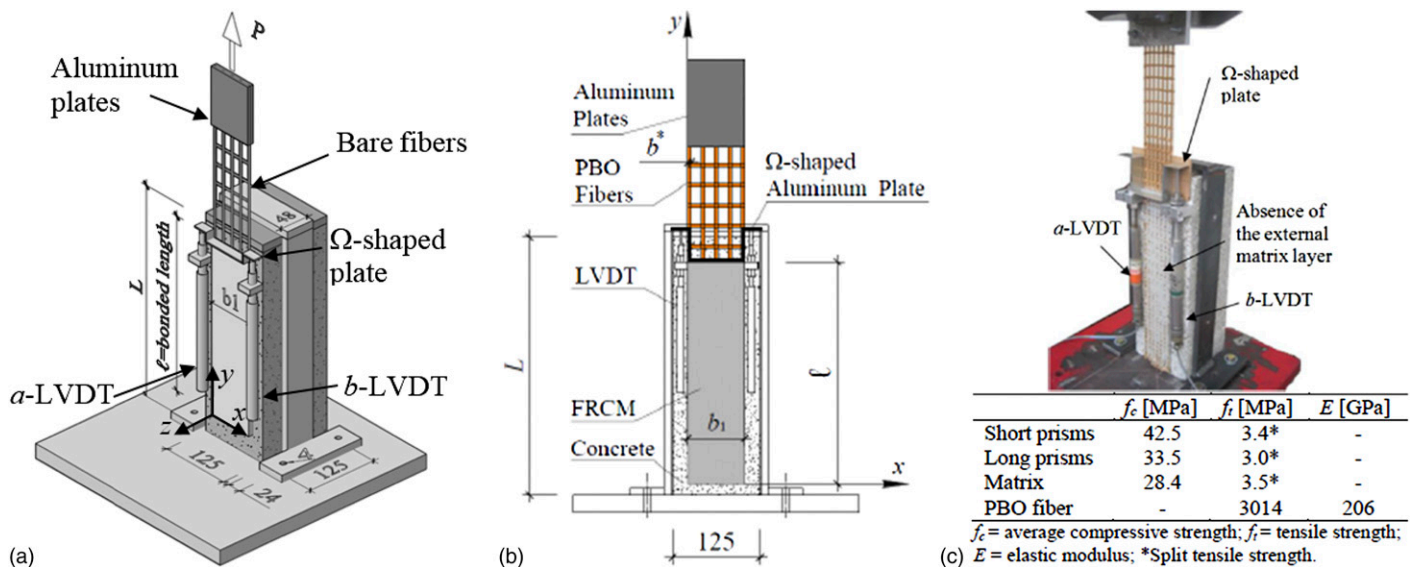
The transversal fiber bundles, which are all located on one side of the longitudinal fiber bundles, were placed against the matrix internal layer for some specimens and against the matrix external layer for others. For some specimens, the external layer of matrix was applied over the PBO fiber net, whereas the fibers were left uncovered for others (Fig. 1(c). The bonded width (b_1) and length (ℓ) of the composite were varied. Two LVDTs were mounted on the concrete surface close to the lateral edges of the composite at the beginning of the bonded area. The LVDTs reacted off of a thin aluminum Ω-shaped bent plate that was attached to the PBO transversal fiber bundle surface adjacent to the beginning of the bonded area as shown in Fig. 1. The average of the two LVDT measurements is defined as the global slip g. All direct-shear tests were conducted in displacement control by increasing the global slip g at a rate equal to 0.00084 mm/s (D'Antino et al. 2014).

In previous works, the authors defined the stress as (D'Antino et al. 2014)

$$\sigma = \frac{P}{nb^*t^*} \tag{1}$$

where P = applied load [Fig. 1(a)]; and n = number of longitudinal fiber bundles. The value of the peak stress $\sigma^* = P^*/(nb^*t^*)$ is obtained from Eq. (1) when the applied load is equal to the peak applied load P^*.

Although a width effect within the single bundle of fibers was observed in the literature (Banholzer 2004; Hartig et al. 2008), the σ^*-b_1 plot showed that a width effect related to the entire composite width does not exist (D'Antino et al. 2014), which is not the case for FRP-concrete joints (Subramaniam et al. 2011). It should be noted that the absence of a global width effect for bonded widths smaller

	f_c [MPa]	f_t [MPa]	E [GPa]
Short prisms	42.5	3.4*	-
Long prisms	33.5	3.0*	-
Matrix	28.4	3.5*	-
PBO fiber	-	3014	206

f_c = average compressive strength; f_t = tensile strength; E = elastic modulus; *Split tensile strength.

Fig. 1. (a and b) Single-lap direct-shear test setup (dimensions in millimeters); (c) specimen DS_330_60_L_D_1 (image by T. D'Antino) and material characteristics

than 34 mm cannot be confirmed by the experiments previously conducted by the authors.

Note on the Notation Adopted in this Paper

For specimens with two layers of matrix, the quantities (such as the fracture energy and the interfacial shear stress) that require a distinction between the internal matrix layer–fiber and external matrix layer–fiber interfaces are indicated with superscripts i and e, respectively. The interface characteristics between the internal layer of matrix and the fibers may vary whether the external layer is present or not. Therefore, the interfacial parameters that refer to the internal matrix layer are indicated with a subscript L for specimens without the external matrix layer, rather than with the superscript i used for the internal matrix layer when both layers are present. A subscript L is also used for the applied load P when referring to specimens without the external matrix layer. The global slip g was increased at the same constant rate independently of the type of specimen; therefore, it is always indicated without the subscript L.

Idealized Applied Load–Global Slip Response

The specimens herein presented failed because of debonding of the fiber net from the embedding matrix. The debonding was characterized by increasing slip at the matrix-fiber interfaces and by the presence of friction for the portion of the bonded area where the fibers were debonded. In this context, the term friction is used to describe the interlocking phenomenon between the fibers or between the fibers and the matrix. In this paper, the term friction and interlocking will be considered as interchangeable, although interlocking might be preferable to avoid confusion with dry friction.

The evidence obtained through the single-lap tests, together with the results available in the literature (Banholzer 2004; Hartig et al. 2008), allowed the authors to propose an idealized applied load–global slip curve (D'Antino et al. 2014), which is reported in Fig. 2. The idealized P-g curve is representative of specimens with and without the external layer of matrix. For the sake of brevity, the curve shown in Fig. 2 refers to specimens with the external matrix layer.

After a first linear branch (OA), the idealized P-g curve becomes nonlinear as a result of the interface microdamage, until the onset of debonding (Point B). The applied load at Point B is also referred to as the debonding load, P_{deb} (or $P_{\mathrm{deb},L}$), or the load-carrying capacity of the matrix-fiber interface. The debonding load P_{deb} (or $P_{\mathrm{deb},L}$) can be achieved only when the composite bonded length, ℓ, is equal to or longer than the effective bond length, l_{eff}, which is the minimum
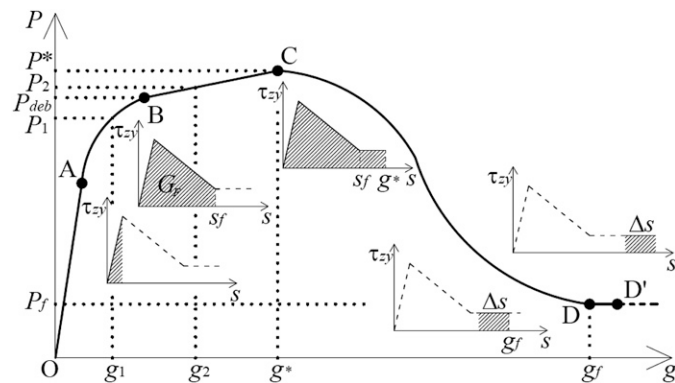

Fig. 2. Idealized load P versus global slip g response

length needed to fully establish the stress-transfer mechanism (D'Antino et al. 2014).

At the onset of debonding (Point B), the portion of the bonded area engaged in the stress transfer corresponds to the part of the bonded region close to the loaded end, and its length is equal to the effective bonded length l_{eff} (if $\ell \geq l_{\mathrm{eff}}$). After Point B, when $\ell > l_{\mathrm{eff}}$, as the interfacial crack propagates, the region engaged in the stress transfer (attributable to bond only) maintains its length equal to l_{eff} as it translates along the bonded length toward the free end. The region that has already debonded behind the stress-transfer zone is subject to friction (interlocking) between single fiber filaments and between fibers and matrix (Banholzer 2004; Hartig et al. 2008), which calls for an increase of the applied load. The applied load increases until it reaches the peak applied load (P^* or P_L^*) at Point C. At Point C ($g = g^*$), the residual bonded length has reached the free end, and its length is still equal to l_{eff}. After Point C, the residual bonded length is less than l_{eff}, and the applied load decreases until the bond mech-anism is no longer present. As a result, the load-transfer capacity of the matrix-fiber interface is provided only by friction (Point D, $g = g_f$). After Point D, the load response becomes constant, and the applied load value is only associated with friction (P_f or $P_{f,L}$). A schematic representation of the translation of the stress-transfer zone can be found in D'Antino et al. (2014). It should be noted that, in the tests conducted by the authors, the fibers extended beyond the bonded area at the free end (Sneed et al. 2014). After Point C, slippage of the fibers at the free end was observed. No measurement of the free end slip was considered in this study.

Seventy-nine direct-shear tests with different bonded lengths, bonded widths, and number of matrix layers are presented in this work. Table 1 reports the name and the corresponding peak load (P^* or P_L^*) for all specimens presented. The nomenclature of the specimens tested is explained in Note 1 of Table 1. Note 2 of Table 1 refers to the analysis of the load redistribution among the fiber bundles, which is presented later in this paper.

Fracture Mechanics Approach

The fracture mechanics approach used for FRP-concrete joints (Carloni and Subramaniam 2012) was extended to the case of FRCM-concrete joints by the authors in a previous publication (D'Antino et al. 2014). In this section, a general approach with different responses of the two matrix-fiber interfaces is presented. A Mode II failure at the matrix-fiber interface is assumed. As a first attempt to study the stress-transfer mechanism between the matrix and the fibers, the deformation of the matrix layers and the concrete substrate is neglected. The assumption of a rigid matrix will be discussed further in a future publication. Digital image correla-tion (DIC) was used to measure the displacement field on the surface of selected specimens to investigate the deformation of the external matrix layer. The results, not included in this work for the sake of brevity, indicate that the deformation of the external layer of matrix is relatively small. In addition, a three-dimensional numerical model of the composite perfectly bonded to the concrete surface was de-veloped in D'Antino (2014). The results showed that the assumption of a rigid matrix is acceptable to study the stress transfer. The free-body diagram of a segment of one fiber bundle is illustrated in Fig. 3. The reference system is shown in Fig. 1(a). Specifically, $y = 0$ and $y = \ell$ correspond to the free and loaded ends of the composite strip, respectively. The slip between the PBO fiber and the matrix interfaces is denoted by s, whereas the axial stress in the fibers and the shear stress at the interfaces are denoted by σ_{yy} and τ_{zy}^j, re-spectively. The superscript j is equal to i or e to indicate the internal or external matrix layer, respectively. As the deformation of the

Table 1. Direct-Shear Test Specimens

Specimen	P^* or P^*_L (kN)	$\sqrt{}$ or $\times$
DS_330_43_L_1	4.96	$\sqrt{}$
DS_330_43_L_2	4.63	$\sqrt{}$
DS_330_43_L_3	4.61	$\sqrt{}$
DS_330_43_L_4	3.98	$\sqrt{}$
DS_330_43_L_5	3.96	$\sqrt{}$
DS_330_43_L_6	3.82	$\sqrt{}$
DS_330_43_L_7^T	2.67	$\times$
DS_330_43_L_8^T	3.67	$\sqrt{}$
DS_330_43_L_9^T	3.09	$\times$
DS_330_43_L_10	4.45	$\times$
DS_330_43_L_11	4.72	$\sqrt{}$
DS_330_43_L_S_1^T	3.24	$\sqrt{}$
DS_330_43_L_S_2	4.69	$\sqrt{}$
DS_330_60_L_1	5.80	$\sqrt{}$
DS_330_60_L_2	5.49	$\sqrt{}$
DS_330_60_L_3	6.60	$\sqrt{}$
DS_330_60_L_4	5.46	$\sqrt{}$
DS_330_60_L_5	5.26	$\sqrt{}$
DS_330_60_L_D_1	5.19	$\sqrt{}$
DS_330_60_L_D_2	6.13	$\sqrt{}$
DS_330_60_L_D_3	5.47	$\sqrt{}$
DS_330_60_L_D_4	4.90	$\sqrt{}$
DS_330_60_L_S_1	5.97	$\sqrt{}$
DS_450_60_L_1	6.90	$\sqrt{}$
DS_450_60_L_2	5.96	$\sqrt{}$
DS_450_60_L_3	6.43	$\times$
DS_450_60_L_4	6.23	$\times$
DS_450_60_L_5	6.91	$\sqrt{}$
DS_330_43_1^T	4.43	$\times$
DS_330_43_2^T	5.25	$\sqrt{}$
DS_330_43_3	5.27	$\sqrt{}$
DS_330_43_5	4.79	$\times$
DS_330_43_6	5.09	$\sqrt{}$
DS_330_43_S_1^T	4.48	$\times$
DS_330_43_S_2^T	5.12	$\sqrt{}$
DS_330_43_S_3^T	3.03	$\sqrt{}$
DS_330_43_S_5	4.03	$\times$
DS_330_60_1^T	7.05	$\sqrt{}$
DS_330_60_2^T	6.56	$\sqrt{}$
DS_330_60_3^T	6.06	$\sqrt{}$
DS_330_60_4^T	6.50	$\sqrt{}$
DS_330_60_5^T	6.28	$\sqrt{}$
DS_330_60_6	7.01	$\times$
DS_330_60_D_1	8.29	$\sqrt{}$
DS_330_60_D_2	7.12	$\sqrt{}$
DS_330_60_D_3	6.56	$\sqrt{}$
DS_330_60_D_4	5.24	$\sqrt{}$
DS_330_60_D_5	6.69	$\sqrt{}$
DS_330_60_S_1	6.30	$\times$
DS_330_60_S_2	7.31	$\sqrt{}$
DS_330_60_S_3	6.55	$\sqrt{}$
DS_330_60_T_1	6.62	$\sqrt{}$
DS_330_60_T_2	6.27	$\sqrt{}$
DS_330_60_T_3	6.59	$\sqrt{}$
DS_330_80_1	8.47	$\sqrt{}$
DS_330_80_2	8.84	$\times$
DS_330_80_3	8.28	$\sqrt{}$
DS_330_80_D_1	8.90	$\sqrt{}$
DS_330_80_D_2	8.68	$\sqrt{}$
DS_330_80_D_3	8.90	$\times$

Table 1. (*Continued.*)

Specimen	P^* or P^*_L (kN)	$\sqrt{}$ or $\times$
DS_330_80_D_4	8.42	$\sqrt{}$
DS_330_80_D_5	8.58	$\sqrt{}$
DS_450_60_1	6.40	$\sqrt{}$
DS_450_60_2	6.34	$\sqrt{}$
DS_450_60_3	6.44	$\times$
DS_450_60_4	5.77	$\sqrt{}$
DS_450_60_5	6.51	$\sqrt{}$
DS_450_60_6	6.79	$\sqrt{}$
DS_450_60_7	6.65	$\sqrt{}$
DS_450_60_D_1	7.01	$\sqrt{}$
DS_450_60_D_2	6.67	$\sqrt{}$
DS_450_60_D_3	7.33	$\sqrt{}$
DS_450_60_S_1	6.63	$\sqrt{}$
DS_450_60_S_2	6.86	$\sqrt{}$
DS_450_80_1	8.62	$\sqrt{}$
DS_450_80_2	9.07	$\sqrt{}$
DS_450_80_3	9.32	$\times$
DS_450_80_4	8.86	$\times$
DS_450_80_5	10.04	$\times$

Note: DS_X_Y_(L, S, T, and/or D)_Z$^{(T)}$, where X = bonded length (ℓ) in millimeters, Y = bonded width (b_1) in millimeters, L = absence of the external layer of matrix, S = presence of strain gauges mounted on the fiber net, T = transversal bundles removed before applying the matrix, D = specimen tested until a constant load at the end of the test was measured, Z = specimen number, and superscript T = fiber net oriented with the transversal fiber bundles directly against the matrix internal layer; $\sqrt{} = \Delta \leq \bar{s}_f$; $\times = \Delta > \bar{s}_f$; P^* = peak load; and P^*_L = peak load of specimens without the external layer of matrix.
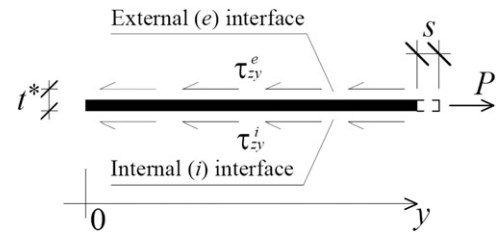
Fig. 3. Free-body diagram of a segment of one fiber bundle

matrix is neglected, the slip s between the fibers and the two layers of matrix is the same. Hence, no superscript j is applied to s.

Given the fiber segment represented in Fig. 3, the work done by the external forces can be written as

$$W_{\text{ext}} = \int_0^{s(y)} P(y)\,ds - b^* \int_0^y \left(\int_{s(0)}^{s(y)} \sum_{j=i,e} \tau_{zy}^j\,ds \right) dy \qquad (2)$$

The slip s is expressed in terms of the axial strain (ε_{yy}) in the fibers

$$s = \int_0^y \varepsilon_{yy}\,dy + s(0) \qquad (3)$$

If the behavior of the fibers is assumed linear elastic and E is the elastic modulus of the fibers, then the external work can be rewritten using Eq. (3) as

$$W_{\text{ext}} = \frac{b^* t^*}{E} \int_0^y \sigma_{yy}^2 \, \mathrm{d}y - b^* \int_0^y \left(\int_{s(0)}^{s(y)} \sum_{j=i,e} \tau_{zy}^j \mathrm{d}s \right) \mathrm{d}y \tag{4}$$

If $\Psi = b^* t^* y$ is the volume of the PBO fiber segment, then the work done by the internal forces is

$$W_{\text{int}} = \int_\Psi \left[\int_0^{\varepsilon_{yy}} \sigma_{yy}(\varepsilon_{yy}) \mathrm{d}\varepsilon_{yy} \right] \mathrm{d}\Psi = \frac{b^* t^*}{2E} \int_0^y \sigma_{yy}^2 \mathrm{d}y \tag{5}$$

Equating the internal and external works yields

$$\frac{b^* t^*}{E} \int_0^y \sigma_{yy}^2 \mathrm{d}y - b^* \int_0^y \left(\int_{s(0)}^{s(y)} \sum_{j=i,e} \tau_{zy}^j \mathrm{d}s \right) \mathrm{d}y = \frac{b^* t^*}{2E} \int_0^y \sigma_{yy}^2 \mathrm{d}y \tag{6}$$

Because Eq. (6) must be satisfied for each y along the bonded length

$$\frac{b^* t^*}{2E} \sigma_{yy}^2 - b^* \int_{s(0)}^{s(y)} \sum_{j=i,e} \tau_{zy}^j \, \mathrm{d}s = 0 \tag{7}$$

Assuming that there is no slip at the free end, i.e., $s(0) = 0$, if $y = l_{\text{eff}}$, then the second term of Eq. (7) is integrated between 0 and $s(l_{\text{eff}}) = s_f$

$$G_F^i = \int_0^{s_f} \tau_{zy}^i \mathrm{d}s \tag{8}$$

$$G_F^e = \int_0^{s_f} \tau_{zy}^e \mathrm{d}s \tag{9}$$

Eqs. (8) and (9) represent the fracture energies needed to create and fully break a unit crack of the internal matrix layer–fiber and external matrix layer–fiber interfaces, respectively. The term fully break refers to the bond mechanism without including friction as discussed in D'Antino et al. (2014).

Fig. 4(a) shows the idealized cohesive material law τ_{zy}^j-s valid for both the internal matrix layer fiber– and external matrix layer–fiber interfaces and put forward by the authors (D'Antino et al. 2014). The idealized cohesive material law depicted in Fig. 4(a) is also representative of the matrix-fiber interface of specimens without the external matrix layer ($\tau_{zy,L}$-s), the parameters of which are indicated within parentheses in Fig. 4. In this paper, it is assumed that $s = s_L$, which implies that the slip is not affected by the absence of the external matrix layer. Debonding occurs when the slip reaches the value s_f. When $s > s_f$, friction (interlocking) between single fiber filaments and between matrix and fibers provides a constant value of the shear stress equal to τ_f^j ($\tau_{f,L}$). Fig. 4(b) represents a simplified τ_{zy}^j-s curve that will be used in the section "Proposed Bond-Slip Relationships" to study the role of the two layers of matrix in the stress transfer.
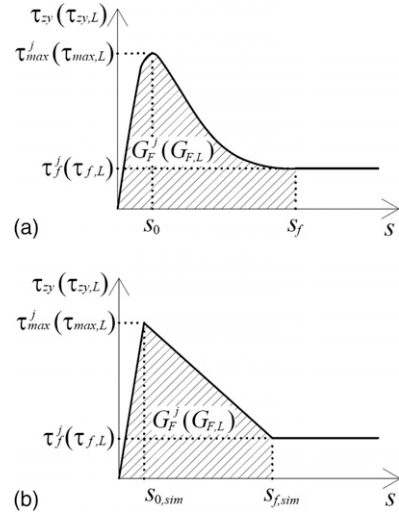
Fig. 4. (a) Idealized shear stress–slip curve; (b) simplified shear stress–slip curve

The relationship between the points of the idealized P-g curve and the area under the τ_{zy}-s curve is shown in Fig. 2, under the hypothesis that $\tau_{zy}^i = \tau_{zy}^e = \tau_{zy}$. A simplified trilinear τ_{zy}-s curve [Fig. 4(b)] is used in Fig. 2. Point A corresponds to the engagement of the linear part of the bond behavior. At Point B, the load is related to the fracture energy of the interface (attributable to the bond only), and at the loaded end, the global slip is equal to the slip s_f, which implies that the interfacial crack has formed. Between Points B and C, the interfacial crack propagates, and the debonded region behind the crack is subject to friction, which calls for an increase of the load related to the area of the bond-slip relation for $s_f \leq s \leq g$. [Note that $g = s(\ell)$.] After Point D, the entire strip of fibers has debonded, and the slip of the fibers increases, which corresponds to a translation of a constant area $\tau_f \Delta s$ under the bond-slip relation for $s > s_f$.

If $y = l_{\text{eff}}$, then $\sigma_{yy} = \sigma_{\text{deb}} = P_{\text{deb}}/(nb^* t^*)$. Eqs. (7)–(9) can be used to derive the debonding load P_{deb}, which is written in Eq. (10) for n fiber bundles, because no width effect related to the entire composite width was observed

$$P_{\text{deb}} = nb^* \sqrt{2Et^* \left(G_F^i + G_F^e \right)} \tag{10}$$

Eq. (10) represents the relationship between the debonding load and the fracture energies G_F^i and G_F^e.

Under the same fracture mechanics approach, the debonding load of n fiber bundles without the external matrix layer can be written as

$$P_{\text{deb},L} = nb^* \sqrt{2Et^* G_{F,L}} \tag{11}$$

where $G_{F,L} = $ fracture energy of the internal matrix layer–fiber interface when the external layer of matrix is not present. It is important to observe that in general, $G_{F,L} \neq G_F^i$; however, in the sections "Results of the Fracture Mechanics Approach" and "Proposed Bond-Slip Relationships" it will be assumed that $G_{F,L} = G_F^i$ in an attempt to determine the cohesive material laws for the two interfaces from the experimental results.

Results of the Fracture Mechanics Approach

In this section, the fracture parameters of the matrix-fiber interface are derived under the assumption that the two matrix-fiber interfaces

have the same role ($\tau_{zy}^i = \tau_{zy}^e = \tau_{zy}$). The fracture parameters are derived directly from the strain measurements along the fiber bundles. This approach was previously used by the authors in D'Antino et al. (2014). Strain gauges were applied directly on the fiber bundles along the bonded length to capture the distribution of the axial strain along the direction of the applied load. Twelve specimens were instrumented with strain gauges applied to the central fiber bundle. The position of the strain gauges can be found in D'Antino et al. (2014).

The strain profiles corresponding to four points of the load response located in a small region around the assumed position of Point B (Fig. 2), which is the unique point along the load response at which the bond mechanism is fully established and friction (interlocking) is not yet present, were considered (D'Antino et al. 2014). The range of load that defines the small region around Point B is named (P_1, P_2) or ($P_{1,L}, P_{2,L}$), whereas the corresponding range of g is termed (g_1, g_2). The average values of the debonding load P_{deb} or $P_{deb,L}$ corresponding to the four points in the region (P_1, P_2) or ($P_{1,L}, P_{2,L}$) are reported in Table 2, as well as the range (P_1, P_2) or ($P_{1,L}, P_{2,L}$) and the range (g_1, g_2).

The strain profiles corresponding to the four points in the P-g curve around Point B (Fig. 2) were approximated using a nonlinear function that takes into account the bond mechanism and friction (interlocking) mechanism after debonding as follows (D'Antino et al. 2014):

$$\varepsilon_{yy} = \varepsilon_0 + \frac{\alpha + ky}{1 + e^{-(y-y_0)/\beta}} \tag{12}$$

The values of ε_0, α, β, and y_0 were determined using nonlinear regression analysis of the measured strains. The parameter k is dependent on whether the strain profile refers to specimens with both the internal and external matrix layers

$$k = \frac{2\overline{\tau}_f}{Et^*} \tag{13a}$$

or to specimens with only the internal matrix layer

$$k = \frac{\overline{\tau}_{f,L}}{Et^*} \tag{13b}$$

where $\overline{\tau}_{f,L}$ and $\overline{\tau}_f$ = average shear stresses associated with friction (interlocking) for specimens with one and two layers of matrix, respectively. Specifically, $\overline{\tau}_f$ and $\overline{\tau}_{f,L}$ are equal to 0.06 and 0.08 MPa, respectively, and were evaluated experimentally according to Eqs. (14a) and (14b), respectively

$$\overline{\tau}_f = \frac{\overline{P}_f}{2nb^*\ell} \tag{14a}$$

$$\overline{\tau}_{f,L} = \frac{\overline{P}_{f,L}}{nb^*\ell} \tag{14b}$$

where $nb^*\ell$ = nominal bonded area of one matrix-fiber interface; and $\overline{P}_f$ and $\overline{P}_{f,L}$ = average of the load values associated with friction (interlocking) between fibers and matrix, which are obtained from those specimens denoted with D [tested until the constant load associated with friction (interlocking) was reached]. The average value of l_{eff}, corresponding to the four points within the small region around Point B for each specimen equipped with strain gauges, is reported in Table 2. Specifically, l_{eff} can be determined from the strain profile as outlined in D'Antino et al. (2014). Under the assumption that l_{eff} is not influenced by the presence of the external matrix layer, the average value for the 11 specimens presented was computed as $\overline{l}_{eff} = 260$ mm (with coefficient of variation 0.084). The value of l_{eff} for specimen DS_330_43_L_S_1[T], not reported in Table 2, was not used to compute the average value $\overline{l}_{eff}$, because the presence of the transversal bundles directly against the internal matrix layer influenced the results as will be explained in the section "Effects of the Transversal Fiber Bundles."

The experimental curve τ_{zy}-s, under the hypothesis that the two layers are assumed to have the same role ($\tau_{zy}^i = \tau_{zy}^e = \tau_{zy}$), was constructed by using the strain profile obtained through the fitting procedure of Eq. (12) and considering the equilibrium condition for an infinitesimal segment of fibers (D'Antino et al. 2014)

$$\tau_{zy} = \tau_{zy}^i = \tau_{zy}^e = \frac{1}{2}Et^*\frac{d\varepsilon_{yy}}{dy} \tag{15}$$

The slip between the fibers and the two layers of matrix was obtained by integrating the strain ε_{yy}[Eq. (3) and $s(0) = 0$]. Hence, the cohesive material law for the interfaces was obtained, and the fracture energy $G_F^i = G_F^e = G_F$ was calculated as the area under the curve τ_{zy}-s for $0 \leq s \leq s_f$. Similarly, for specimens without the external matrix layer, the $\tau_{zy,L}$-s curve was obtained directly from the strain profiles of those specimens equipped with strain gauges and without the external matrix layer. It should be noted that the shear stress $\tau_{zy,L}$, for those specimens without the external layer of matrix, was calculated from Eq. (15) without considering the factor $1/2$. Fig. 4(a) shows the shape of the τ_{zy}-s and $\tau_{zy,L}$-s curves associated with the strain profile described in Eq. (12). Examples of experimental τ_{zy}-s curves obtained from the strain profiles following the aforementioned procedure can be found in D'Antino et al. (2014).

Table 2. Results of the Fracture Mechanics Analysis ($G_F^i = G_F^e = G_F$)

Specimen	l_{eff} (mm)	(g_1, g_2) (mm)	(P_1, P_2) or ($P_{1,L}, P_{2,L}$) (kN)	P_{deb} or $P_{deb,L}$ (kN)	G_F^{fit} or $G_{F,L}^{fit}$ (J/m²)
DS_330_43_L_S_2	250	(1,2, 1.4)	(4.13, 4.23)	4.18	880
DS_330_43_S_1[T]	300	(1.7, 2.3)	(3.90, 4.11)	3.96	450
DS_330_43_S_2[T]	280	(1.5, 1.8)	(3.98, 4.39)	4.17	680
DS_330_43_S_3[T]	280	(1.2, 1.5)	(2.63, 2.72)	2.71	240
DS_330_43_S_5	230	(0.7, 1.0)	(3.42, 3.64)	3.51	300
DS_330_60_S_1	260	(0.9, 1.2)	(5.51, 5.91)	5.74	360
DS_330_60_S_2	225	(0.7, 0.9)	(6.49, 6.75)	6.65	550
DS_330_60_S_3	240	(1.1, 1.4)	(5.63, 5.90)	5.75	470
DS_330_60_L_S_1	250	(1.0, 1.4)	(5.67, 5.91)	5.80	950
DS_450_60_S_1	255	(1.1, 1.3)	(5.50, 5.91)	5.70	540
DS_450_60_S_2	255	(0.9, 1.1)	(5.67, 5.91)	5.77	430

The experimental values of the fracture energy are termed G_F^{fit} and $G_{F,L}^{\text{fit}}$ to indicate that they were derived through the strain fitting of Eq. (12), and their average values for the four points of the load response are reported in Table 2 for each specimen equipped with strain gauges. The theoretical debonding load for the specimens reported in Table 2, obtained through Eq. (10) ($G_F^i = G_F^e = G_F$) and Eq. (11), is in good agreement with the corresponding experimental debonding load (Table 2).

Distribution of Applied Load among Bundles

The different impregnation of the matrix along the fiber bundles caused a different behavior and performance of the fiber bundles in some specimens, which in turn resulted in a nonuniform distribution of the applied load among the bundles. The nonuniform load distribution, evidenced by a rigid rotation of the Ω-shaped plate, had a strong influence on the test results and especially on the peak loads P^* and P_L^* (Sneed et al. 2014).

The load redistribution among bundles was studied by comparing the displacements, g_a and g_b, measured by the two LVDTs used to control the test. The points of the Ω-shaped plate off of which the LVDTs tips reacted had a distance h from the edges of the composite strip (Fig. 5). Simple geometrical relations were used to compute the displacements corresponding to the edge of the composite strip, termed g_a^L and g_b^R (Fig. 5). In Fig. 5, r defines the center of rotation measured from the left edge of the composite strip, h is the distance between the edge of the composite and the centerline of the adjacent LVDT, and d is the distance between the centerlines of the LVDTs.

The P-g_a, P-g_b, P_L-g_a, and P_L-g_b curves obtained from the two LVDTs were plotted to compare their behavior. In addition, the difference between the displacements at the two edges of the composite $\Delta = |g_a^L - g_b^R|$ was computed for the entire range of g for all specimens. To define a limit beyond which the nonuniform load distribution compromised the results reliability, the τ_{zy}-s and $\tau_{zy,L}$-s curves obtained from the strain analysis described in the "Results of the Fracture Mechanics Approach" section were employed. The values of the slip corresponding to the peak shear stress, s_0, and to the complete debonding of the fibers, s_f, were collected from the 11 tests reported in Table 2. The average values are $\bar{s}_0 = 0.18$ mm and $\bar{s}_f = 1.57$ mm. The average values were obtained by considering together all specimens with one or two layers of matrix. Only those specimens for which $\Delta \leq \bar{s}_f$ for $P \leq P^*$ and $P_L \leq P_L^*$ were considered reliable and used for the following analysis, whereas the others were disregarded. This criterion was adopted to ensure that, at the peak load (P^* or P_L^*), if the residual bonded length was equal to l_{eff} for the bundle on one edge of the composite, then the bundle on the other edge was still bonded for a length greater than l_{eff}. The criterion adopted in this work is not unique, and further results are necessary to evaluate if other criteria can be used. Specimens for which $\Delta \leq \bar{s}_f$ for $P \leq P^*$ and $P_L \leq P_L^*$ are marked with a check symbol ($\sqrt{}$) in
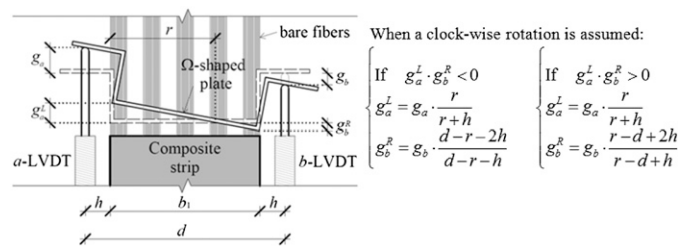
Table 1, whereas specimens for which $\Delta > \bar{s}_f$ for $P \leq P^*$ and $P_L \leq P_L^*$ are marked with a cross symbol ($\times$). Sixty-two specimens were considered reliable (78% of all specimens reported in Table 1), whereas 17 specimens were disregarded (22% of all specimens reported in Table 1). Only 10 specimens reported $\Delta \leq \bar{s}_0$ for $P \leq P^*$ and $P_L \leq P_L^*$.

Fig. 6 shows, as an example, the P-g_a and P-g_b curves for one reliable specimen [DS_450_60_D_1, Fig. 6(a)] and one disregarded specimen [DS_450_60_3, Fig. 6(b)]. The corresponding P-g curves are plotted with a light-gray line for reference. When $\Delta \leq \bar{s}_f$, the P-g_a and P-g_b curves are plotted with a black line, whereas when $\Delta > \bar{s}_f$, the same curves are depicted with a dark gray line. A black dot marks the points for which $\Delta = \bar{s}_f$. Fig. 6(a) shows one of the specimens that were tested until complete debonding of the fiber net from the matrix. It can be observed that, for specimen DS_450_60_D_1 [Fig. 6(a)], the applied load reached the constant value corresponding to P_f, as reported in the idealized P-g curve (Fig. 2).

Effects of the Transversal Fiber Bundles

Twelve of the 79 specimens presented in this work were cast with the transversal fiber bundles directly against the internal matrix layer (specimens denoted with a superscript T after the sequential number in Table 1). Sixty-four of the 67 remaining specimens had the longitudinal fiber bundles directly against the internal matrix layer, whereas for three specimens, the transversal bundles were removed prior to applying the matrix layers (specimens with a T before the
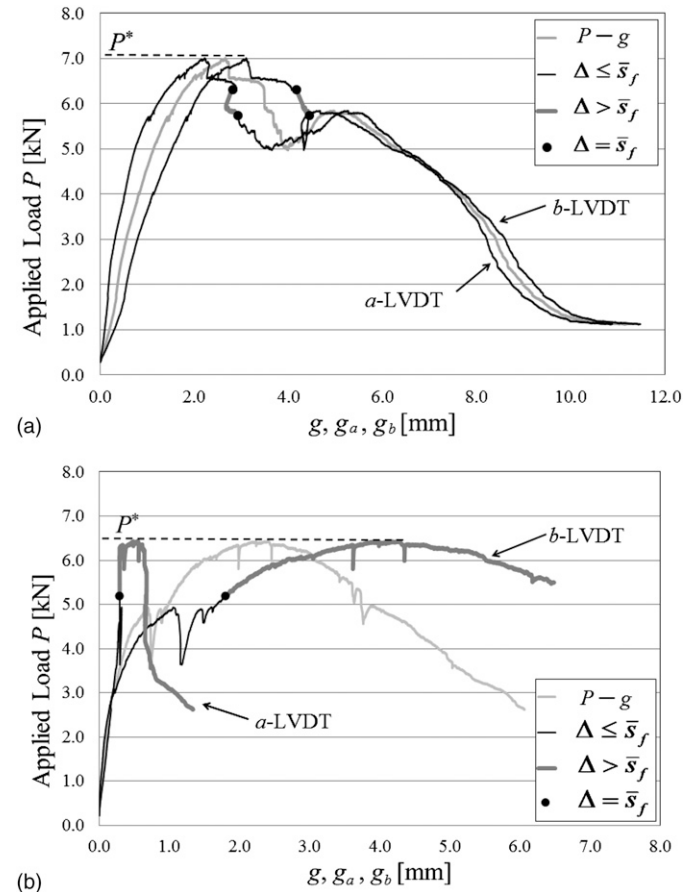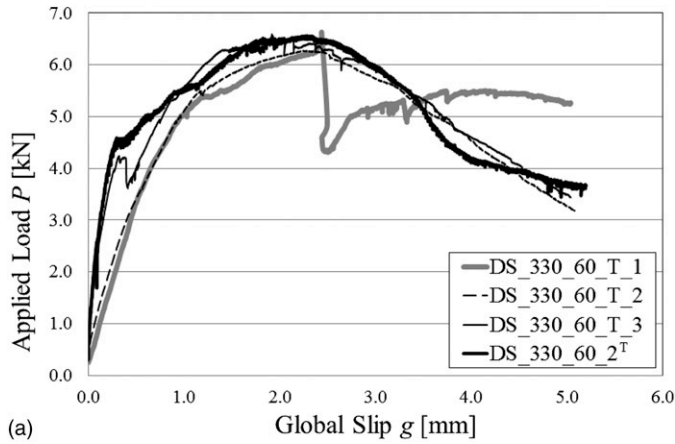
Fig. 6. Applied load P versus LVDT measurements for (a) specimen DS_450_60_D_1; (b) specimen DS_450_60_3

Fig. 5. Position of the LVDTs

sequential number in Table 1). A photograph of the fiber longitudinal bundles after the removal of the transversal bundles is shown in Fig. 7(b).

The specimens with the external matrix layer and without the transversal fiber bundles, DS_330_60_T_1, DS_330_60_T_2, and DS_330_60_T_3, presented the same behavior as the specimens with the external matrix layer and the transversal fiber bundles placed directly against either the matrix external or internal layer. Furthermore, for all three specimens without the transversal bundles, $\Delta \leq \bar{s}_f$ for $P \leq P^*$ (i.e., square root symbol in Table 1). The load responses of these specimens are particularly important, because they confirm that the matrix external layer provides a different contribution with respect to the matrix internal layer even when the bond between the longitudinal fiber bundles and the matrix is not interrupted by the transversal fiber bundles. Fig. 7(a) reports the load responses of the specimens without the transversal fiber bundles and of specimen DS_330_60_2^T for comparison. The P-g_a and P-g_b curves of specimen DS_330_60_T_3 are reported in Fig. 7(b) with the corresponding P-g plot for comparison.

Specimens that are considered as reliable (i.e., square root symbol in Table 1) with two layers of matrix, bonded length $\ell = 330$ mm, and different widths were compared in terms of the peak stress σ^*. An 8% difference was observed when comparing the average of σ^* between specimens with the transversal bundles placed against the internal matrix layer and specimens with the transversal bundles placed against the external matrix layer. This

(a)
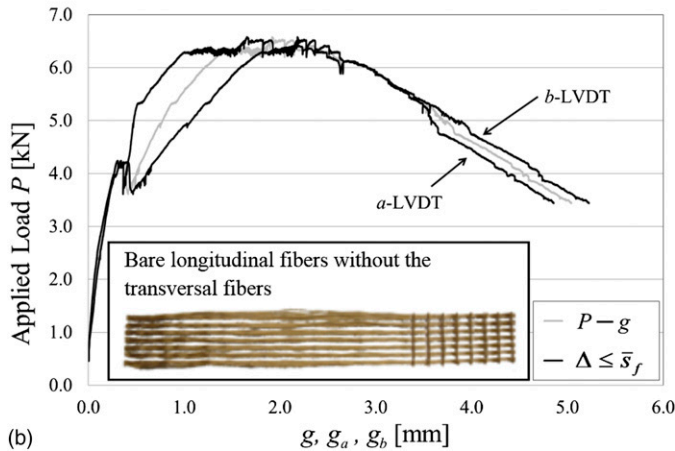
(b)

Fig. 7. (a) P-g curves of specimens without the transversal bundles and DS_330_60_2^T for comparison; (b) applied load P versus LVDT measurements for specimen DS_330_60_T_3

indicates that, when both layers of matrix are present, the peak stress is not significantly influenced by the position of the transversal bundles. Further, the results obtained considering only reliable specimens with bonded length $\ell = 330$ mm showed that, for specimens with two layers of matrix, the presence of the transversal bundles against either the internal or the external matrix layer appears to have no influence if compared with the three specimens without the transversal bundles (3% difference in terms of average of the peak stress σ^*). When comparing the peak stress σ_L^* of reliable specimens that have bonded length $\ell = 330$ mm and that have the transversal bundles placed against the internal matrix layer versus those that have the longitudinal bundles placed against the internal matrix layer, it can be noted that the position of the transversal fiber bundles influences the peak stress σ_L^* (18% of difference). This effect, observed by the authors in a previous publication without distinguishing between reliable and not reliable specimens (Sneed et al. 2014), is affected by the limited number of reliable specimens without the external matrix layer and with the transversal bundles placed against the internal matrix layer. It is interesting to notice that, when the fiber bundles are placed against the internal layer and both layers are present, the peak load is not significantly affected.

Role of the Internal and External Matrix Layers in the Stress-Transfer Mechanics

The discussion of the experimental results relative to the reliable specimens indicates that the two layers of matrix have a different role. The debonding loads for all reliable specimens with two layers of matrix (P_{deb}) and without the external layer of matrix ($P_{deb,L}$) can be obtained by

$$P_{deb} = P^* - \bar{\tau}_f 2nb^* \left(\ell - \bar{l}_{eff}\right) \tag{16a}$$

$$P_{deb,L} = P_L^* - \bar{\tau}_{f,L} nb^* \left(\ell - \bar{l}_{eff}\right) \tag{16b}$$

Both values $\bar{\tau}_f = 0.06$ MPa and $\bar{\tau}_{f,L} = 0.08$ MPa, introduced earlier via Eqs. (14a) and (14b), were obtained by including all specimens marked with square root and multiplication symbols and denoted with a D (Table 1). In fact, when the fibers are completely debonded from the matrix, the applied load was assumed to be evenly distributed across the composite width. The ratio of the debonding loads can be introduced in terms of stresses

$$\eta_{deb} = \sigma_{deb,L} / \sigma_{deb} \tag{17}$$

where $\sigma_{deb,L} = P_{deb,L}/(nb^*t^*)$ and $\sigma_{deb} = P_{deb}/(nb^*t^*)$.

If Eqs. (10) and (11) are employed and it is assumed that $G_F^i = G_{F,L}$, which implies that the interfacial behavior between the fibers and the internal matrix layer is not influenced by the presence of the external matrix layer, then Eq. (18) provides the ratio between fracture energies associated with the internal and external matrix–fiber interfaces

$$\frac{G_F^i}{G_F^e} = \frac{\eta_{deb}^2}{\left(1 - \eta_{deb}^2\right)} \tag{18}$$

Given the results of the reliable specimens tested (i.e., square root in Table 1), Eq. (18) provided a value of $\eta_{deb} = 0.93$, which calls for a ratio between the internal- and external-layer fracture energy equal to $G_F^i / G_F^e = 6.40$. It should be noted that Eq. (18) can be applied only if the stress-transfer mechanism is fully established at the internal and external matrix–fiber interfaces simultaneously. Because

the fracture energy is independent of the shape of the shear stress–slip function, Eq. (18) does not provide information on the τ_{zy}^{j}-s curves.

Proposed Bond-Slip Relationships

The results of the fracture mechanics approach were presented earlier considering the contributions of the internal and external matrix layers as equal. Although the results in terms of the load-carrying capacity are in good agreement with experimental values (D'Antino et al. 2014), such an approach may not be able to provide accurate results in the case of multilayer strengthening applications, because it does not take into account the different contributions to the load-carrying capacity of the external matrix layers with respect to the internal matrix layer.

In an attempt to investigate the different roles of the external and internal matrix layers, the authors introduced the ratio between the internal and external fracture energies, G_F^i and G_F^e, through Eqs. (17) and (18). The ratio was obtained under the assumption that $G_F^i = G_{F,L}$. In this section, the same assumption is adopted to further study the role of the internal and external matrix layers and identify the fracture parameters needed to describe the τ_{zy}^{j}-s curves. In this section, it is also assumed that $\tau_{zy}^i = \tau_{zy,L}$ and $s = s_L$, which implies that the shape of the cohesive material law of the internal matrix layer–fiber interface is not influenced by the presence of the external matrix layer.

In this section, the hypothesis that $\tau_{zy}^i = \tau_{zy}^e$ is removed to describe the different roles of the two matrix layers with two different cohesive material laws. Because the fracture energies G_F^j do not depend on the shape of the corresponding τ_{zy}^j-s curves, each of the shear stress–slip curves can be simplified into a three-branch linear relationship with the same corresponding fracture energy [Fig. 4(b)]. The subscript sim, which is adopted in Fig. 4(b) to indicate values of the simplified shear stress–slip curve, is omitted in this section.

The simplified τ_{zy}^i-s curve for the internal layer was derived from the experimental $\tau_{zy,L}$-s curves obtained from the strain measurements of the specimens equipped with strain gauges and without the external matrix layers. Only those (two) specimens without the external layer and marked with a square root in Table 1 were considered. Specimen DS_330_43_L_S_1^T was not considered, because the transversal fiber bundles were placed against the internal matrix layer. To build the simplified τ_{zy}^i-s curve, the maximum shear stress τ_{max}^i, the frictional shear stress τ_f^i, and the slope of the linear ascending part were kept the same for the experimental and simplified curves. The maximum shear stress τ_{max}^i and the slope of the linear ascending part of the simplified τ_{zy}^i-s curve were obtained as the average values of the corresponding values of the experimental $\tau_{zy,L}$-s curves of specimens DS_330_43_L_S_2 and DS_330_60_L_S_1. Eq. (14b) was used to compute the average of the shear stress τ_f^i ($\tau_f^i = \tau_{f,L}$) of specimens DS_330_43_L_S_2 and DS_330_60_L_S_1. The corresponding slip s_f for the simplified curve was obtained by imposing that the fracture energy G_F^i was equal for the curve associated with the strain profiles described in Eq. (12) and the simplified curves (Fig. 4).

Eq. (18) was used to identify the simplified τ_{zy}^e-s curve for the external matrix layer, provided that $\tau_f^e = 2\overline{\tau}_f - \overline{\tau}_{f,L}$. Three different theoretical models for the simplified τ_{zy}^e-s curve are proposed in this section. Fig. 8 shows the three models and the necessary conditions to determine the parameters of the external matrix layer–fiber interface.

It should be noted that if the matrix layers are considered rigid and Model C is applied, then the ratio provided by Eq. (18) should be adjusted, because the denominator would include not only the fracture energy of the external matrix layer–fiber interface but also a friction (interlocking) contribution, which corresponds to the area under the τ_{zy}^e-s curve from s_f^e to s_f^i [Fig. 8(c)]. The fracture parameters of the simplified curves are listed in Table 3.

Conclusions

The experimental and analytical investigation of the PBO FRCM-concrete interface was presented in this paper. The stress-transfer mechanism between the PBO fibers and the cementitious matrix was investigated through the application of a fracture mechanics approach. Based on the experimental evidence and the discussion presented, the following conclusions can be drawn.

1. The load response of specimens with both the internal and external matrix layers is not affected by the orientation of the transversal fiber bundles. However, for specimens without the
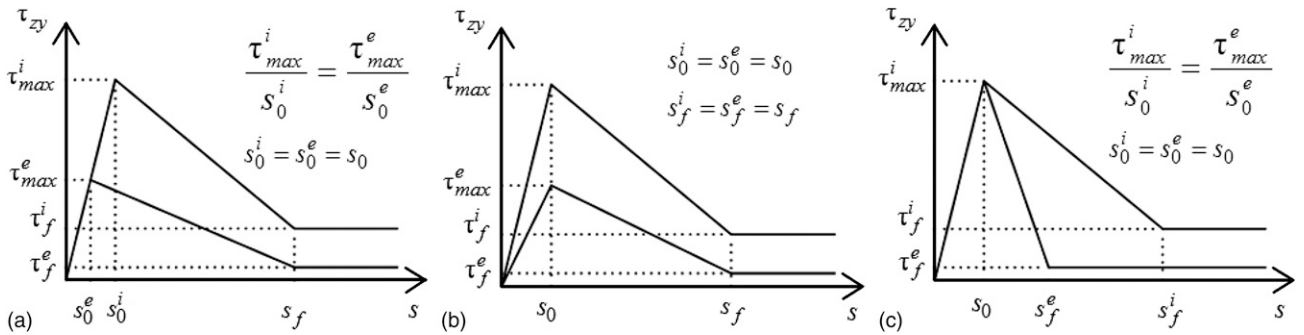

Fig. 8. Proposed shear stress versus slip curves according to (a) Model A; (b) Model B; (c) Model C

Table 3. Internal and External Shear Stress and Corresponding Slip for the Proposed Shear Stress–Slip Relationships

Model	τ_{max}^i (MPa)	s_0^i (mm)	τ_{max}^e (MPa)	s_0^e (mm)	τ_f^i (MPa)	s_f^i (mm)	τ_f^e (MPa)	s_f^e (mm)
A	1.68	0.08	0.24	0.01	0.08	1.04	0.04	1.04
B	1.68	0.08	0.24	0.08	0.08	1.04	0.04	1.04
C	1.68	0.08	1.68	0.08	0.08	1.04	0.04	0.17

external matrix layer, the presence of the transversal bundles against the internal matrix layer influences the load response.

2. Under the assumption that the presence of the external matrix layer does not influence the behavior of the internal matrix layer, the role of the two layers of matrix can be expressed by the ratio of the fracture energies associated with the internal matrix layer–fiber and external matrix layer–fiber interfaces.

3. Simplified shear stress–slip relationships are proposed to describe the behavior of the internal and external matrix layers, which can be used to investigate the stress-transfer mechanism at the different matrix-fiber interfaces.

References

Banholzer, B. (2004). "Bond behavior of multi-filament yarn embedded in a cementitious matrix." Ph.D. thesis, Rheinisch-Westfälische Technische Hochschule (RETH) Aachen Univ., Aachen, Germany.

Carloni, C., Sneed, L. H., and D'Antino, T. (2013). "Interfacial bond characteristics of fiber reinforced cementitious matrix for external strengthening of reinforced concrete members." *Proc., 8th Int. Conf. on Fracture Mechanics of Concrete and Concrete Structures*, J. G. M. Van Mier et al., eds., Barcelona International Center for Numerical Methods in Engineering, Barcelona, Spain, 129–137.

Carloni, C., and Subramaniam, K. V. (2012). "Application of fracture mechanics to debonding of FRP from RC members." *A fracture approach for FRP-concrete structures*, American Concrete Institute, Farmington Hills, MI, 10-1–10-14.

Carrara, P., and Ferretti, D. (2013). "A finite-difference model with mixed interface laws for shear tests of FRP plates bonded to concrete." *Composites Part B*, 54(Nov), 329–342.

Carrara, P., Ferretti, D., Freddi, F., and Rosati, G. (2011). "Shear tests of carbon fiber plates bonded to concrete with control of snap-back." *Eng. Fract. Mech.*, 78(15), 2663–2678.

D'Ambrisi, A., Feo, L., and Focacci, F. (2012). "Bond-slip relations for PBO-FRCM materials externally bonded to concrete." *Composites Part B*, 43(8), 2938–2949.

D'Ambrisi, A., Feo, L., and Focacci, F. (2013a). "Experimental analysis on bond between PBO-FRCM strengthening materials and concrete." *Composites Part B*, 44(1), 524–532.

D'Ambrisi, A., and Focacci, F. (2011). "Flexural strengthening of RC beams with cement-based composites." *J. Compos. Constr.*, 10.1061/(ASCE) CC.1943-5614.0000218, 707–720.

D'Ambrisi, A., Focacci, F., and Caporale, A. (2013b). "Strengthening of masonry–unreinforced concrete railway bridges with PBO-FRCM materials." *Compos. Struct.*, 102(Aug), 193–204.

D'Antino, T. (2014). "Bond behavior in fiber reinforced polymer composites and fiber reinforced cementitious matrix composites." Ph.D. thesis, Univ. of Padova, Padova, Italy.

D'Antino, T., Carloni, C., Sneed, L. H., and Pellegrino, C. (2014). "Matrix–fiber bond behavior in PBO FRCM composites: A fracture mechanics approach." *Eng. Fract. Mech.*, 117(Feb), 94–111.

D'Antino, T., Sneed, L. H., Carloni, C., and Pellegrino, C. (2013). "Bond behavior of the FRCM-concrete interface." *Proc., 11th Int. Symp. on Fiber Reinforced Polymers for Reinforced Concrete Structures* (CD-ROM), J. Barros and J. Sena-Cruz, eds., Univ. Minho, Guimarães, Portugal, 1–10.

Grace, C., Yang, Y., and Sneed, L. H. (2012). "Fracture mechanics approach to predicting the behavior of reinforced concrete members with externally-bonded fiber reinforced polymer laminates." *A fracture approach for FRP-concrete structures*, American Concrete Institute, Farmington Hills, MI, 7-1–7-20.

Hartig, J., Häußler-Combe, U., and Schicktanz, K. (2008). "Influence of bond properties on the tensile behaviour of textile reinforced concrete." *Cement Concr. Compos.*, 30(10), 898–906.

Ombres, L. (2012). "Debonding analysis of reinforced concrete beams strengthened with fibre reinforced cementitious mortar." *Eng. Fract. Mech.*, 81(Feb), 94–109.

Pellegrino, C., and D'Antino, T. (2013). "Experimental behaviour of existing precast prestressed reinforced concrete elements strengthened with cementitious composites." *Composites Part B*, 55(Dec), 31–40. Pellegrino, C., and Modena, C. (2009). "Influence of FRP axial rigidity on FRP-concrete bond behaviour: An analytical study." *Adv. Struct. Eng.*, 12(5), 639–649.

Salomoni, V., Mazzucco, G., Pellegrino, C., and Majorana, C. (2011). "Three-dimensional modelling of bond behaviour between concrete and FRP reinforcement." *Eng. Comput.*, 28(1), 5–29.

Sneed, L. H., D'Antino, T., and Carloni, C. (2014). "Investigation of bond behavior of PBO fiber-reinforced cementitious matrix composite-concrete interface." *ACI Mater. J.*, 111(1–6), 1–12.

Subramaniam, K. V., Carloni, C., and Nobile, L. (2011). "An understanding of the width effect in FRP–concrete debonding." *Strain*, 47(2), 127–137.

Täljsten, B., and Blanksvärd, T. (2007). "Mineral-based bonding of carbon FRP to strengthen concrete structures." *J. Compos. Constr.*, 10.1061/(ASCE)1090-0268(2007)11:2(120), 120–128.

Toutanji, H., and Deng, Y. (2007). "Comparison between organic and in organic matrices for RC beams strengthened with carbon fiber sheets." *J. Compos. Constr.*, 10.1061/(ASCE)1090-0268(2007)11:5(507), 507–513.